

# Applicability of Taylor's hypothesis in thermally-driven turbulence

Abhishek Kumar<sup>1,\*</sup> and Mahendra K. Verma<sup>1,†</sup>

<sup>1</sup>*Department of Physics, Indian Institute of Technology, Kanpur, India 208016*

In this paper, we show that in the presence of large-scale circulation (LSC), Taylor's hypothesis can be invoked to deduce the energy spectrum in thermal convection using real space probes, a popular experimental tool. We perform numerical simulation of turbulent convection in a cube and observe that the velocity field follows Kolmogorov's spectrum ( $k^{-5/3}$ ). We also record the velocity time series using real space probes near the lateral walls. The corresponding frequency spectrum exhibits Kolmogorov's spectrum ( $f^{-5/3}$ ), thus validating Taylor's hypothesis with the steady LSC playing the role of a mean velocity field. The aforementioned findings based on real space probes provide valuable inputs for experimental measurements used for studying the spectrum of convective turbulence.

## I. INTRODUCTION

Thermal convection exhibits a wide range of phenomena—instabilities, patterns, chaos, and turbulence, depending on the strength of the buoyancy force. An idealized system called *Rayleigh-Bénard convection* (RBC) [1–5] in which a thin layer of fluid is heated from below and cooled from the top captures the aforementioned complexity. Turbulent convection, a topic of this article, remains largely unsolved despite a century of efforts. In this paper, we discuss the spectral properties of the velocity field in RBC. The two important parameters of RBC are the Rayleigh number, which is defined as the ratio of the buoyancy and the viscous term, and the Prandtl number, which is the ratio of the kinematic viscosity and thermal diffusivity.

For isotropic hydrodynamic turbulence, Kolmogorov [6] showed that one-dimensional energy spectrum  $E(k) = C\epsilon^{2/3}k^{-5/3}$ , called Kolmogorov spectrum, for the intermediate range of wavenumbers ( $k$ ). Here  $\epsilon$  is the energy flux, and  $C$  is the Kolmogorov's constant. For buoyancy-driven turbulence with stable stratification, Bolgiano [7] and Obukhov [8] argued that in the wavenumber band  $k < k_B$ ,  $E(k) \sim k^{-11/5}$  for the velocity field and  $E_T(k) \sim k^{-7/5}$  for the temperature field, but in the wavenumber band  $k_B < k < k_d$ , both velocity and temperature fields exhibit Kolmogorov's spectrum. Here  $k_B, k_d$  are the Bolgiano and Kolmogorov's wavenumber respectively. The steepening of the velocity spectrum for  $k < k_B$  is due to the conversion of the kinetic energy to the potential energy that depletes the energy flux to yield  $\Pi(k) \sim k^{-4/5}$  [7, 8].

Procaccia and Zeitak [9] and L'vov and Falkovich [10] argued that the aforementioned Bolgiano-Obukhov phenomenology of stably stratified turbulence also applies to RBC. Recently Kumar *et al.* [11] showed that the turbulence phenomenology of RBC differs significantly from that of stably stratified turbulence; in RBC, the

temperature field feeds the kinetic energy, hence the kinetic energy flux is a nondecreasing function of wavenumber, rather than decreasing as  $k^{-4/5}$ . For unit Prandtl number, numerical simulations of Kumar *et al.* [11] show that the viscous dissipation becomes effective at lower wavenumbers itself and it balances the energy feed by buoyancy. Hence, the kinetic energy flux becomes constant that leads to Kolmogorov's spectrum for RBC. A shell model for RBC [12] also confirms the above observations, albeit at larger Rayleigh numbers.

To probe turbulence in thermal convection, scientists measure and analyze the velocity and temperature fields in experiments. The determination of the energy spectrum  $E(k)$  requires complete three-dimensional high-resolution real-space data, which is difficult to record at present. Only a handful experiments captured two-dimensional (2D) high-resolution velocity field using 2D particle image velocimetry [see 13–16]; an approximate energy spectrum is computed from such data under the assumption of homogeneity and isotropy, which is not strictly valid in convection. In most experiments, the velocity field,  $u_z(t)$ , and/or temperature field,  $T(t)$ , are probed at fixed points in the flow [e.g., 17–23].

In a fluid moving with a constant velocity  $\mathbf{U}_0$ , Taylor's hypothesis [24] is invoked to relate the frequency power spectrum,  $E(f) = |u(f)|^2/2$ , to one-dimensional wavenumber spectrum  $E(k)$  using  $E(f) = E(k)(2\pi)/U_0$  since  $f = U_0 k/(2\pi)$ . In Appendix A, we show that in hydrodynamic turbulence with significantly large  $U_0$ ,  $E(k) \sim k^{-5/3}$  and  $E(f) \sim f^{-5/3}$  in accordance with Taylor's hypothesis. In addition,  $E(k) \approx \tilde{E}(\tilde{f})$  with appropriate scaling—the frequency  $f \rightarrow \tilde{f} = f(2\pi)/U_0$  and  $E(f) \rightarrow \tilde{E}(\tilde{f}) = E(f)U_0/(2\pi)$  (see Appendix A for details). However, for homogeneous and isotropic turbulence with  $\mathbf{U}_0 = 0$ , we show that  $E(f) \sim f^{-2}$  since  $f \sim \epsilon^{1/3}k^{2/3}$  from Kolmogorov's theory [25, 26]. In a related development, Cholemaris and Arakeri [27] proposed a model to relate spatial and temporal Eulerian two-point correlations which is applicable in the absence of mean flow; the above computation retains the effects of sweeping by the large eddies.

Unfortunately, thermal convection in a box does not have a mean velocity  $\mathbf{U}_0$ ; hence an application of Taylor's

\* abhishek.kir@gmail.com

† mkv@iitk.ac.in

hypothesis to convective turbulence has been intensely debated [see 4, 5]. To advance understanding of this phenomenon, He *et al.* [28] and He and Zhang [29] employed the elliptic model to relate space-time correlation function in RBC to spatial and temporal separations between probes. Using experimental data, they showed that the flow is swept in a combined manner by the random velocity and the mean velocity field and that the frequency spectrum of the temperature field  $E_T(f) \sim f^{-1.35}$ .

A lack of clarity in the application of Taylor’s hypothesis for convective turbulence is one of the biggest stumbling blocks for understanding convective turbulence, especially for the spectra of the velocity and temperature fields. Chillà *et al.* [18] and Zhou and Xia [20] measured the time series of the temperature field in convection experiments on water and reported Bolgiano-Obukhov scaling. Wu *et al.* [17] also reported Bolgiano-Obukhov scaling from the frequency spectrum of the temperature field for helium gas. Castaing [30] and Cioni *et al.* [19] however reported Kolmogorov’s scaling for the temperature field in the helium gas and mercury experiments respectively. Shang and Xia [23] and Mashiko *et al.* [31] reported Bolgiano-Obukhov scaling from the time series of the velocity field of water and mercury respectively. Ashkenazi and Steinberg [32] performed an experiment with sulphur hexafluoride ( $\text{SF}_6$ ) gas and reported Bolgiano-Obukhov scaling in the frequency spectra for both temperature and velocity fields. Niemela *et al.* [22] reported a dual scaling, as predicted by Bolgiano and Obukhov, from the probe measurement of the temperature field for helium gas. Skrbek *et al.* [21] computed the temperature structure functions in time domain with the cryogenic helium gas as working fluid and obtained scaling exponents in the Bolgiano regime. Using the above data, Bershadskii *et al.* [33] obtained  $E_T(f) \sim f^{-1.37}$  which they relate to the Clusterization and intermittency. There are similar variations in the velocity field exponent as well [23]. Apart from the time-domain measurements, space-domain measurements were also carried by the researchers [13–16] using 2D PIV. Sun *et al.* [13] observed Kolmogorov’s scaling in the central region of the cell for water. Kunnen *et al.* [15] analyzed the scaling of structure function for water and observed Bolgiano-Obukhov scaling. The scaling of energy spectrum for convective turbulence has also been studied by creating density difference in a long vertical tube [34]. Pawar and Arakeri [35] created density difference by using the brine in bottom tank and fresh water in the top tank and achieved  $\text{Ra} \approx 10^{10}$  with  $\text{Pr} \approx 600$  and shows KO scaling for the velocity field and BO scaling for the concentration fluctuation. The above results indicate significant uncertainties on the determination of the spectrum of convective turbulence.

Numerical simulations of RBC provide a better picture of the energy spectrum since the complete velocity field is available for analysis. Grossmann and Lohse [36] performed the simulation for  $\text{Pr} = 1$  under Fourier-Weierstrass approximation and reported Kolmogorov’s scaling. Based on periodic boundary condition, Borue

and Orszag [37] and Škandera *et al.* [38] reported Kolmogorov’s scaling for the velocity and temperature fields. Rincon [39] performed simulation for  $\text{Pr} = 1$  and  $\text{Ra} = 10^6$  using a higher order finite-difference scheme. He employed the  $\text{SO}(3)$  analysis to treat isotropic and anisotropic projections of the structure function, but his analysis was inconclusive in identifying any definite spectral slope. For zero and small Prandtl numbers, Mishra and Verma [40] showed that  $E(k) \sim k^{-5/3}$  since the buoyancy is essentially concentrated near the low wavenumbers for such flows, similar to that in hydrodynamic turbulence that exhibits  $k^{-5/3}$  energy spectrum.

Verzicco and Camussi [41] and Camussi and Verzicco [42] performed numerical simulation in a cylindrical geometry and collected the data from the real space probe. The frequency spectrum from numerical data exhibit Bolgiano-Obukhov scaling. Interestingly, Calzavarini *et al.* [43] observed both Bolgiano-Obukhov and Kolmogorov’s spectra in the boundary layer and bulk respectively. Kaczorowski and Xia [44] performed the simulation for  $\text{Pr} = 0.7$  and  $4.38$  for Rayleigh number ranging from  $10^5$  to  $10^9$  and reported KO scaling for the longitudinal velocity structure functions, but BO scaling for the temperature structure functions in the center of the cubical cell. Kerr [45] performed the simulation for  $\text{Pr} \approx 1$  on a  $288 \times 288 \times 96$  grid in a cubical box using Chebyshev based pseudospectral method under no-slip boundary conditions; he reported the horizontal spectrum as a function of horizontal wavenumber  $k_\perp = \sqrt{k_x^2 + k_y^2}$  and observed Kolmogorov’s spectrum. As discussed earlier, Kumar *et al.* [11] showed Kolmogorov’s spectrum along with a constant energy flux, thus confirming Kolmogorov’s theory for convective turbulence. Recently Nath *et al.* [46] showed that the convective turbulence is weakly anisotropic.

In this paper, we perform numerical simulation of RBC in a cubical container that contains a *steady large-scale circulation* (LSC) [47–51]. For the velocity field, we compute the wavenumber spectrum, as well as the frequency spectrum from the time series measured by a set of real-space probes. We show that both these spectra follow Kolmogorov’s  $k^{-5/3}$  spectrum. Taylor’s hypothesis is valid for such system due to the “local” constant velocity near the lateral walls.

The outline of the paper is as follows. In Sec. II we set up our governing equations. In Sec. III we explain our simulation methods and discuss the results of our numerical simulations in Sec. IV. We conclude in Sec. V.

## II. GOVERNING EQUATIONS

The dynamical equations that describe RBC under Boussinesq approximation are

$$\frac{\partial \mathbf{u}}{\partial t} + (\mathbf{u} \cdot \nabla) \mathbf{u} = -\frac{1}{\rho_0} \nabla p + \alpha g T \hat{z} + \nu \nabla^2 \mathbf{u}, \quad (1)$$

$$\frac{\partial T}{\partial t} + (\mathbf{u} \cdot \nabla) T = \kappa \nabla^2 T, \quad (2)$$

$$\nabla \cdot \mathbf{u} = 0, \quad (3)$$

where  $\mathbf{u}$  and  $T$  are the velocity and temperature fields respectively, and  $\hat{z}$  is the buoyancy direction. Here  $\alpha$  is the thermal expansion coefficient,  $g$  is the acceleration due to gravity, and  $p$  is the pressure field, and  $\rho_0$ ,  $\nu$ ,  $\kappa$  are the fluid's mean density, kinetic viscosity, and thermal diffusivity respectively.

It is convenient to work with nondimensionalized equations. We nondimensionalize Eqs. (1)-(3) using  $d$  as the length scale, the large-scale velocity  $(\alpha g \Delta d)^{1/2}$  as velocity scale, and  $\Delta$  as the temperature scale, where  $\Delta$  and  $d$  are the temperature difference and the distance between the plates respectively. The eddy turnover time is the time scale of our simulation. The nondimensional equations are

$$\frac{\partial \mathbf{u}}{\partial t} + (\mathbf{u} \cdot \nabla) \mathbf{u} = -\nabla p + T \hat{z} + \sqrt{\frac{\text{Pr}}{\text{Ra}}} \nabla^2 \mathbf{u}, \quad (4)$$

$$\frac{\partial T}{\partial t} + (\mathbf{u} \cdot \nabla) T = \frac{1}{\sqrt{\text{RaPr}}} \nabla^2 T, \quad (5)$$

$$\nabla \cdot \mathbf{u} = 0. \quad (6)$$

The two nondimensional control parameters are the Prandtl number  $\text{Pr} = \nu/\kappa$  and the Rayleigh number  $\text{Ra} = \alpha g \Delta d^3 / (\nu \kappa)$ .

In this paper we solve the above equations numerically and study the energy spectrum for the velocity field in wavenumber space:

$$E(k) = \sum_{k-1 < k' \leq k} \frac{1}{2} |\hat{\mathbf{u}}(\mathbf{k}')|^2. \quad (7)$$

Then we compare  $E(k)$  with the frequency spectrum computed using the time series measured by the real space probes. For better averaging, we employ multiple number of probes in the neighborhood and take the average of the measured signal as

$$u_i(t) = \frac{1}{n} \sum_k u_{i,l}(t), \quad (8)$$

where  $i$  stands for the velocity component ( $i = x, y, z$ ), and  $l$  stands for the probe index. We compute the frequency spectrum  $E(f)$  of the velocity field as

$$E(f) = \frac{1}{2} (|\hat{u}_x(f)|^2 + |\hat{u}_y(f)|^2 + |\hat{u}_z(f)|^2), \quad (9)$$

where  $\hat{u}_i$  is the Fourier transform of the  $i$ -th component of the velocity field.

Another important quantity of RBC is the kinetic energy flux  $\Pi(k_0)$ , which is defined as the kinetic energy

leaving a wavenumber sphere of radius  $k_0$  due to non-linear interactions. The kinetic energy flux is computed using the formula [52, 53]

$$\Pi(k_0) = \sum_{k > k_0} \sum_{p \leq k_0} \Im([\mathbf{k} \cdot \mathbf{u}(\mathbf{k} - \mathbf{p})][\mathbf{u}^*(\mathbf{k}) \cdot \mathbf{u}(\mathbf{p})]). \quad (10)$$

In Kolmogorov's theory of turbulence,  $\Pi(k_0)$  is a constant in the inertial range, and it is equal to the viscous dissipation rate.

### III. SIMULATION METHODS

Equations (4)-(6) are solved in a closed cubical box of unit dimension using an open-source finite-volume code OpenFOAM [54]. We employ the no-slip boundary condition for the velocity field at all the walls, conducting boundary conditions for the temperature field at the horizontal wall, and insulating boundary condition at the vertical wall. Gaussian finite volume integration is used for the computation of derivative terms ( $\nabla p$ , convective, and Laplacian). Gaussian integration is based on a sum of the values of a function on the cell faces; these values are interpolated from the cell centers to the nodes. These data at the cell centers are interpolated using linear interpolation. For time stepping we use second order Crank-Nicolson scheme.

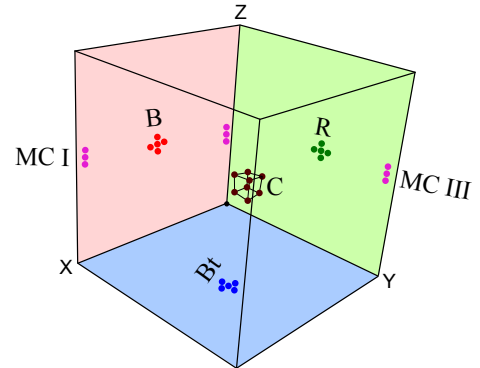


FIG. 1. The real space probe locations in the three-dimensional cubical box of our simulation. The probe locations are labeled as the front (F), back (B), left (L), right (R), top (T), bottom (Bt), middle corners (MC-I, MC-II, MC-III, MC-IV), and center (C) respectively. There are 5 probes near the wall centers, 3 probes in the middle corners, and 9 probes at the center & vertices of a small cube placed at the center of the cube.

We perform simulation for  $\text{Pr} = 1$  (close to that of air) and  $\text{Ra} = 10^8$ . The grid resolution of our simulation is  $256^3$  in a nonuniform mesh with a higher grid concentration near the boundaries in order to resolve the boundary layer. The Reynolds number  $\text{Re}$  for this run is approximately 1634. An important response parameter for the

convective turbulence is the Nusselt number  $Nu$ , which is the ratio of the total (convective plus conductive) heat flux and the conductive heat flux. For the aforementioned simulation,  $Nu \approx 34.4$ . We employ a constant  $\Delta t = 10^{-3}$  for which the Courant number is less than unity, hence our simulation is well resolved in time. Here  $t = 1$  of our simulation corresponds to  $d/\sqrt{\alpha g \Delta d}$ . Note that the aforementioned constant  $\Delta t$  helps us compute the Fourier transform of the real space data using equispaced FFT.

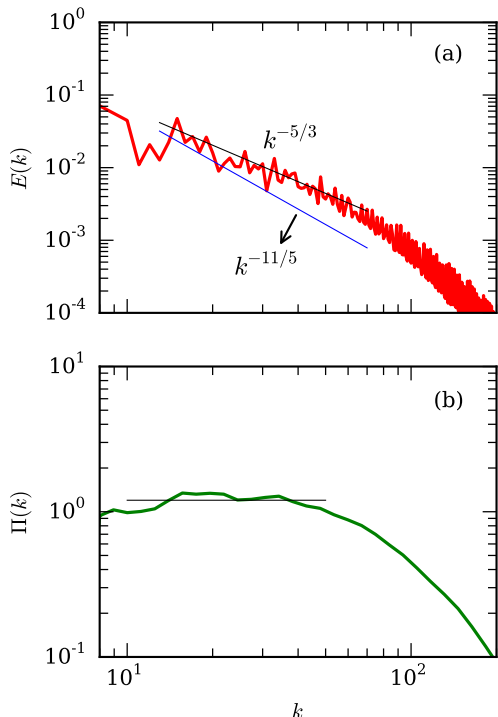


FIG. 2. For RBC with Prandtl number  $Pr = 1$  and Rayleigh number  $Ra = 10^8$ : (a) the kinetic energy spectrum  $E(k)$  with  $k^{-5/3}$  being a better fit than  $k^{-11/5}$ ; (b) the kinetic energy flux  $\Pi(k)$ .

We make a nonuniform mesh such that the width of the smallest cell  $\Delta_{min} = 0.0027$ , and the width of the largest cell  $\Delta_{max} = 0.0054$ . Thus the expansion ratio is  $\Delta_{max}/\Delta_{min} = 2$ . According to Grötzbach condition [55], the mean grid size should be less than  $\pi$  times the Kolmogorov and thermal diffusion length scales. For unit  $Pr$ , the Kolmogorov and thermal diffusion length scales are equal, and they are estimated using the formula  $\eta = L(Pr^2/(RaNu))^{1/4} \approx 0.0041$ , where  $L$  is the box size. Thus  $\pi\eta = 0.013$ , hence  $\Delta_{min}$  and  $\Delta_{max}$  are less than  $\pi\eta$ .

Another important requirement for the DNS is based on the resolution of the thermal boundary layer (BL) [41, 55–58]. Grötzbach [55] recommends at least two to three points in the BL. Verzicco and Camussi [41] and Amati *et al.* [56] however proposed more than three grid points

inside the thermal BL. We estimate the width of the boundary layer using the formula  $\delta \sim 1/(2Nu)$ , in which we keep six points. Thus grid resolution is sufficient for our simulation. We perform grid-independence and  $\Delta t$ -independence tests of our DNS. The Nusselt numbers computed on  $280^3$  and  $300^3$  differ by less than 3% from the simulation on  $256^3$ . Similarly, the Nusselt numbers computed using  $\Delta t = 3 \times 10^{-4}$ ,  $5 \times 10^{-4}$ , and  $\Delta t = 10^{-3}$ , differ from each other by less than 2%.

A primary objective of the present paper is to test Taylor’s hypothesis. For the same, we place real-space probes to record time series of the velocity field using which we compute the frequency spectrum  $E(f)$ . To relate our simulations with experiments, we place real space probes near the middle of the six wall, near the middle of the corner edges, and in the middle of the cube. We label these probes as front (F), back (B), left (L), right (R), top (T), bottom (Bt), middle corners (MC-I, MC-II, MC-III, MC-IV), and center (C) respectively. The number of probes near the wall centers, middle corners, and cubic centers are 5, 3, and 9 respectively. In Fig. 1 we exhibit the probes at B, R, Bt, MC I, MC III, MC IV, and C.

We record the three components of the velocity field at all the real space probes. We run our simulation for 80 time units with constant  $\Delta t = 10^{-3}$ . We record the velocity fields at every 10 steps; thus we have  $8 \times 10^3$  data points. Then we perform Fourier transform of the velocity components  $u_i(t)$  and compute the frequency spectrum  $E(f)$ .

In the next section, we will discuss our results based on the numerical data. We will focus on the computation of  $E(k)$  and  $E(f)$ .

#### IV. RESULTS

We interpolate the real space simulation data to a uniform mesh of  $256^3$  grids, and then perform Fourier transform using FFT that yields energy spectrum  $[E(k)]$  in the wavenumber space. Fig. 2(a) demonstrates that the spectrum is Kolmogorov-like,  $E(k) = C\epsilon^{2/3}k^{-5/3}$  with  $C \approx 1.8$ . We also compute the energy flux using the Fourier modes [53]. The energy flux  $\Pi(k)$  plotted in Fig. 2(b) shows a constant flux in the inertial range. Thus, our simulation exhibits Kolmogorov’s spectrum for RBC, in agreement with the results of Kumar *et al.* [11] and Kumar and Verma [12].

Thermal plumes and large-scale structures are prominent in thermal convection. A snapshot of the flow structure in Fig. 3 exhibits ascending hot plumes (red) and descending cold plumes (blue). To obtain further details, we analyze the flow velocity at different sections. The three vertical sections exhibited in Fig. 4(a)-(c) clearly demonstrate a *large-scale circulation* (LSC) [47–51] with two sets of dominant rolls: in the first roll shown in Fig. 4(a), the hot plumes ascend along the right wall, and the cold plumes descend along the left wall; in the second roll shown in Fig. 4(b), the aforementioned process oc-



TABLE I. For RBC with  $\text{Pr} = 1$  and  $\text{Ra} = 10^8$ , the most energetic 5 modes of the flow.  $E(\mathbf{k}) = |\hat{u}(\mathbf{k})|^2/2$  denotes the modal kinetic energy of the Fourier mode  $(k_x, k_y, k_z)$ .

$(k_x, k_y, k_z)$	$E(\mathbf{k}) =  \hat{u}(\mathbf{k}) ^2/2$
$(1, 0, 1)$	$1.4 \times 10^{-1}$
$(0, 1, 1)$	$6.8 \times 10^{-2}$
$(1, 1, 2)$	$2.9 \times 10^{-3}$
$(1, 3, 3)$	$1.4 \times 10^{-3}$
$(1, 2, 2)$	$1.2 \times 10^{-3}$

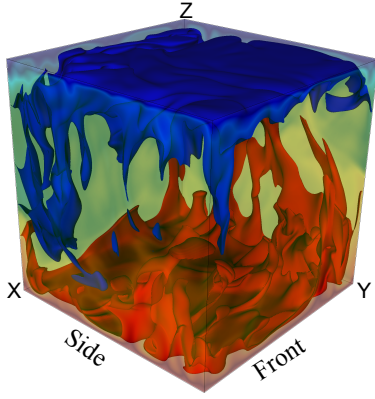


FIG. 3. Temperature isosurfaces exhibiting ascending hot plumes (red) and descending cold plume (blue) for RBC with  $\text{Pr} = 1$  and  $\text{Ra} = 10^8$ .

curs along the front and back walls. These two rolls are described by the most energetic velocity Fourier modes  $(k_x, k_y, k_z) = (1, 0, 1)$  and  $(0, 1, 1)$  respectively. The next three most energetic Fourier modes are  $(1, 1, 2)$ ,  $(1, 3, 3)$ , and  $(1, 2, 2)$ , but their energies are one order of magnitude lower than those of  $(1, 0, 1)$  and  $(0, 1, 1)$  modes (see Table I).

Note that the superposition of these modes leads to a strong flow profile in the diagonal plane shown in Fig. 4(c), but a weak flow profile on the opposite diagonal. The steady LSC is also evident in the movie of Supplementary Material [59]. The presence of LSC suggests that Taylor's hypothesis may be applicable to turbulent convection. Here the velocity of the mean flow acts as approximate  $U_0$ .

In the left column of Fig. 5, we exhibit the time series

$$u_z(t) = \frac{1}{n} \sum_l u_{z,l}(t), \quad (11)$$

measured at L, R, F, B, MC-I, MC-III and C (see Fig. 1). Here  $n$  is the number of local probes which are indexed

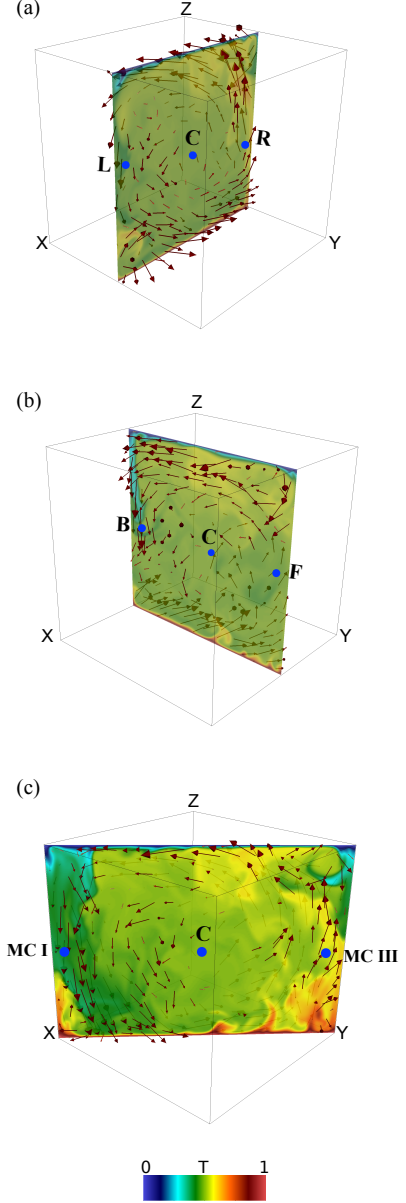


FIG. 4. For RBC with  $\text{Pr} = 1$  and  $\text{Ra} = 10^8$ : (a)  $xz$  roll with hot plumes ascending along the right wall and cold plumes descending along the left wall (b) similar  $yz$  roll. (c) Superposition of the two rolls yields diagonal circulation. The corresponding movie for (c) is in the Supplementary Material [59]. The color convention of the movie is same as of the present figure.

as  $l$ . Note that  $u_z(t)$  is averaged over all the neighbors, e.g.,  $u_z(t)$  at B is averaged over the 5 probes shown in Fig. 1. Here time is in the units of  $d/\sqrt{\alpha g \Delta d}$ . We observe that  $u_z(t)$  of the side walls and corners fluctuate around the mean values of the LSC. However,  $u_z(t)$  of the center probes fluctuate around zero, which is due to the absence

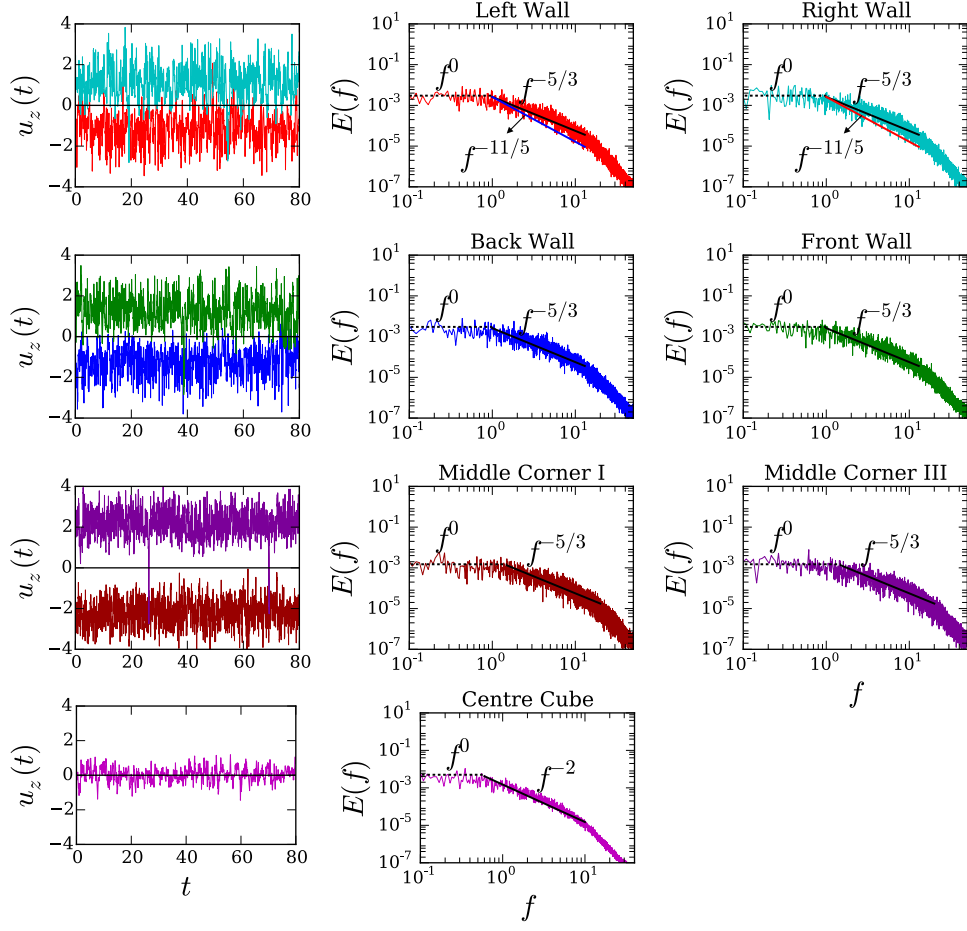


FIG. 5. For RBC with  $\text{Pr} = 1$  and  $\text{Ra} = 10^8$ , time series  $u_z(t)$  measured by the probes, and their corresponding frequency spectra. Left panel: time series for the probes at the left-right walls, back-front walls, middle corners I-III, and center probes (see Fig. 1). Here time  $t$  is in the units of  $d/\sqrt{\alpha g \Delta d}$ . Middle and right panels: The frequency spectrum  $E(f)$  computed for the corresponding probes;  $E(f) \sim f^{-5/3}$  fits better than  $f^{-11/5}$  for the probes at the side walls and middle corners. For the center of the cube,  $E(f) \sim f^{-2}$ . Low-frequency spectrum  $E(f) \sim f^0$  (white noise).

of any mean velocity at the center of the cube.

We compute the frequency spectra of the time series as in Eq. (9), which are depicted in the middle and right panels of Fig. 5 for various set of probes. We observe that  $E(f)$  is noisier than  $E(k)$ ; the smoothness of  $E(k)$  is due to averaging over the modes of a wavenumber shell. For the probes at the side walls and mid corners,  $E(f) \sim f^{-5/3}$ , consistent with the Kolmogorov's phenomenology and Taylor's hypothesis (see middle and right panels of Fig. 5). Here, the LSC acts as a carrier of the fluctuations. Thus we show that Taylor's hypothesis can be employed to the RBC turbulence in the presence of a steady LSC.

In Fig. 6, we simultaneously plot the wavenumber spectrum and the frequency spectrum at the left wall (see Fig. 5) with appropriate scaling—the frequency  $f \rightarrow \tilde{f} = f(2\pi)/U_0$  and  $E(f) \rightarrow \tilde{E}(\tilde{f}) = E(f)U_0/(2\pi)$ . Motivated by the time series  $u_z(t)$  of Fig. 5, we take  $U_0 = 1$ . We observe that both the spectra exhibit Kolmogorov's

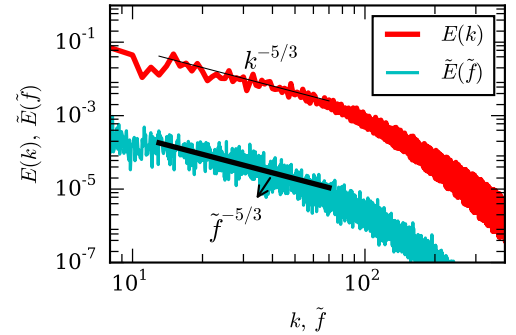


FIG. 6. For RBC with  $\text{Pr} = 1$  and  $\text{Ra} = 10^8$ , plot of the wavenumber spectrum  $E(k)$  and scaled frequency spectrum of the probe at the left wall (see Fig. 5):  $f \rightarrow \tilde{f} = f(2\pi)/U_0$  and  $E(f) \rightarrow \tilde{E}(\tilde{f}) = E(f)U_0/(2\pi)$ . We take  $U_0 = 1$ .

spectrum, but  $\tilde{E}(\tilde{f})$  is several orders of magnitude lower than  $E(k)$  in contrast to hydrodynamic turbulence where  $\tilde{E}(\tilde{f}) \approx E(k)$  (see Appendix A). This is because an LSC roll (one among several LSC rolls) sweeps associated fluctuations with it. For example, the mode  $\mathbf{u}(1, 0, 1)$  advects fluctuations in  $xz$  plane (measured at left and right walls). Similarly, the mode  $\mathbf{u}(0, 1, 1)$  advects fluctuations in  $yz$  plane corresponding to the back and front walls. As a result,  $\tilde{E}(\tilde{f}) \ll E(k)$  because  $E(k)$  is sum of all the fluctuations, but  $\tilde{E}(\tilde{f})$  of Fig. 6 is that of only the left wall that corresponds to the mode  $\mathbf{u}(0, 1, 1)$ . For a homogeneous and isotropic fluid turbulence,  $\mathbf{U}_0$  advects all forms of random fluctuations, that is, random fluctuations of arbitrary directions criss-cross the probe during its measurement, thus yielding  $\tilde{E}(\tilde{f}) \approx E(k)$  for hydrodynamic turbulence (see Appendix A).

There are several RBC experiments in rectangular geometry [18, 60–65]. Our finding is in agreement with the experimental results of Chillà *et al.* [18], which was carried out in a rectangular cell with water as a working fluid. They showed that the frequency and wavenumber spectra of the temperature field are approximately equal in the presence of mean flow.

Our results demonstrate that Taylor’s hypothesis is applicable to turbulent convection in the presence of a steady LSC. Note however that LSC in many experiments are not steady. In a cylinder, Niemela *et al.* [47], Sreenivasan *et al.* [48], Brown *et al.* [49], Xi and Xia [50], and Mishra *et al.* [51] observed azimuthal movement of the LSC, as well flow reversals. Hence, Taylor’s hypothesis may be questionable for such geometries, and we may not be able to relate  $E(f)$  and  $E(k)$  in a straightforward manner.

The center probe, however, exhibits  $E(f) \sim f^{-2}$  due to the absence of LSC; this result is same as  $E(f) \sim f^{-2}$  observed for the hydrodynamic turbulence with  $\mathbf{U}_0 = 0$  [25, 26] (see Appendix A). Another interesting feature of  $E(f)$  is the robust  $f^0$  spectrum (white noise) observed at lower frequencies (see Fig. 5). This feature indicates that the fluctuations at time scales  $t \gtrsim 1$  (corresponding to  $f \lesssim 1$ ) are uncorrelated. This behavior is in sharp contrast to  $E(f) \sim f^{-1}$  reported in experiments exhibiting flow reversals [49, 66]. The difference is possibly due to the variance of the long-time correlations for reversing and non-reversing velocity signals.

## V. CONCLUSIONS

We performed the direct numerical simulation of Rayleigh-Bénard convection in a closed cubical box for  $\text{Pr} = 1$  and  $\text{Ra} = 10^8$  and studied the energy spectrum using the numerical data in space-domain and time-domain. We placed the real space probes in the simulation box and measured the time series of the velocity field. For the velocity field, the wavenumber energy spectrum as well as the frequency spectrum exhibit Kolmogorov’s spectrum. We observe that the kinetic energy

flux is constant. These observations demonstrate that RBC has a similar scaling as of hydrodynamic turbulence, rather than Bolgiano-Obukhov’s scaling. Earlier, Kumar *et al.* [11] had observed similar results in their spectral simulations.

The analysis of the flow structures of RBC and their associated Fourier modes demonstrate the presence of a steady large-scale circulation (LSC) in the flow. Such a mean flow enables an application of Taylor’s hypothesis to turbulent convection, which is why both  $E(k)$  and  $E(f)$  show Kolmogorov’s spectrum. We remark that an azimuthal movement or reversal of the LSC may make such application questionable.

In summary, our numerical simulation of RBC in a cube demonstrates Kolmogorov’s spectrum for both wavenumber and frequency spectra. The correspondence between the two spectra is due to the *steady large-scale circulation* and Taylor’s hypothesis.

## ACKNOWLEDGEMENTS

We thank Sagar Chakraborty for valuable suggestions. Our numerical simulations were performed on *HPC* and *Chaos* clusters of IIT Kanpur. This work was supported by a research grants (Grant No. SERB/F/3279) from Science and Engineering Research Board, India and (Grant No. PLANEX/PHY/2015239) from Indian Space Research Organisation, India.

## Appendix A: Taylor’s hypothesis in hydrodynamic turbulence

The dynamical equations for the incompressible velocity field are

$$\frac{\partial \mathbf{u}}{\partial t} + (\mathbf{U}_0 \cdot \nabla) \mathbf{u} + (\mathbf{u} \cdot \nabla) \mathbf{u} = -\frac{1}{\rho_0} \nabla p + \nu \nabla^2 \mathbf{u} + \mathbf{f}, \quad (\text{A1})$$

$$\nabla \cdot \mathbf{u} = 0, \quad (\text{A2})$$

where  $\mathbf{u}$ ,  $p$ ,  $\mathbf{f}$  are the velocity, pressure, and external force fields respectively, and  $\nu$  is the kinematic viscosity. To test Taylor’s hypothesis for hydrodynamic turbulence, we numerically solve the above equations with  $\mathbf{U}_0 = 0$  in a periodic box of dimension  $(2\pi)^3$  using a pseudospectral code Tarang [67]. In the simulation, we employed a random forcing [68] to the flow in the wavenumber band  $1 \leq k \leq 3$  on  $512^3$  grid. We also use a fourth-order Runge-Kutta scheme for time stepping and 2/3 rule for aliasing. We continue our simulation till it reaches a steady state. Once a steady state is reached, we initiate two new runs with  $\mathbf{U}_0 = 0$  and  $\mathbf{U}_0 = 10\hat{z}$  using the above final state as the initial condition. We carry out the two simulations till  $t = 1$ , where time units is  $2\pi/u_{\text{rms}}$ . Here  $u_{\text{rms}}$  is the rms velocity of the flow, computed as the volume average of the magnitude of the velocity field.

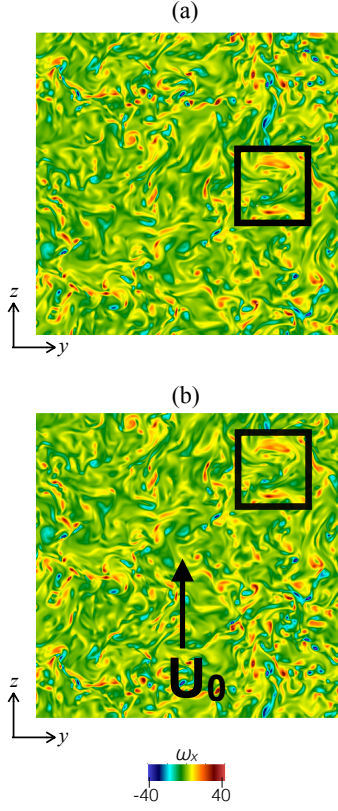


FIG. 7. For hydrodynamic turbulence simulation with  $\text{Re} \approx 1100$ , and  $\mathbf{U}_0 = 0$  and  $\mathbf{U}_0 = 10\hat{z}$ : The density plots of the vorticity component  $\omega_x$  of a vertical cross-section for (a)  $\mathbf{U}_0 = 0$  and (b)  $\mathbf{U}_0 = 10\hat{z}$ . The flow in (b) is shifted upward by  $\mathbf{U}_0\tau$  compared to (a).

The Reynolds number of the flows  $\text{Re} = UL/\nu \approx 1100$ , where  $L, U$  are respectively the length and velocity scales of the flow. In Fig. 7, we illustrate the vorticity component  $\omega_x$  at the same cross-section and the same time in the two boxes. Figure 7(b) is an upward translation by  $\mathbf{U}_0\tau$ , where  $\tau$  is the time interval, of Fig. 7(a), thus indicating a vertical motion of the flow due to  $\mathbf{U}_0$ . We compute the energy spectrum  $E(k)$  and the energy flux  $\Pi(k)$  for both the datasets. As expected, these quantities are identical for both the boxes, and they are plotted in Fig. 8(a,b) respectively. In the inertial range, we observe Kolmogorov's spectrum.

We record the time series of the velocity field at 50 random locations, and then compute their frequency spectra  $E(f)$ . Figs. 9(a,b) exhibit the averaged  $E(f)$  computed using the time series recorded by 50 randomly-located real-space probes for  $\mathbf{U}_0 = 0$  and  $\mathbf{U}_0 = 10\hat{z}$  respectively. For  $\mathbf{U}_0 = 10\hat{z}$ ,  $E(f) \sim f^{-5/3}$ , in accordance with Taylor's hypothesis [24, 26] since  $2\pi f = U_0 k$ . However, for homogeneous and isotropic turbulence with  $\mathbf{U}_0 = 0$ , we obtain  $E(f) \sim f^{-2}$  since  $f \sim \epsilon^{1/3} k^{2/3}$  from Kolmogorov's theory [25]. Interestingly, we also observe  $E(f) \sim f^{-2}$  for small  $U_0$  when  $\epsilon^{1/3} k^{2/3} > U_0 k$  (see Fig. 9(b) for  $U_0 = 0.4\hat{z}$ ).

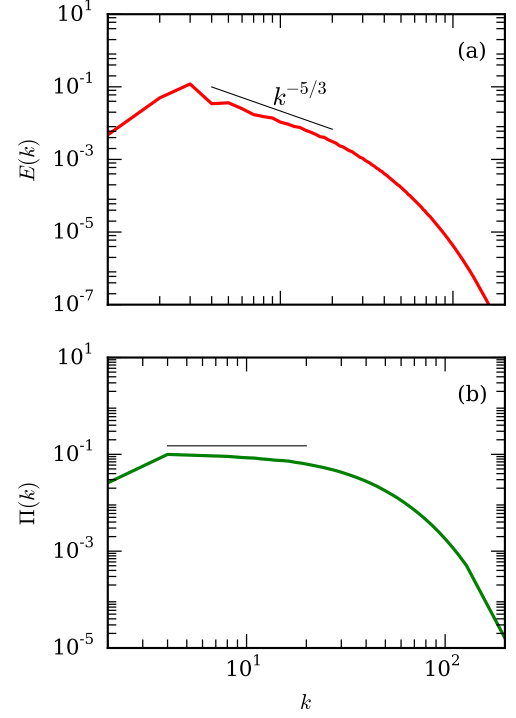


FIG. 8. For hydrodynamic turbulence simulation with  $\text{Re} \approx 1100$ , and  $\mathbf{U}_0 = 0$  and  $\mathbf{U}_0 = 10\hat{z}$ : (a) energy spectra and (b) energy fluxes are the same for both the flows; they follow Kolmogorov's model.

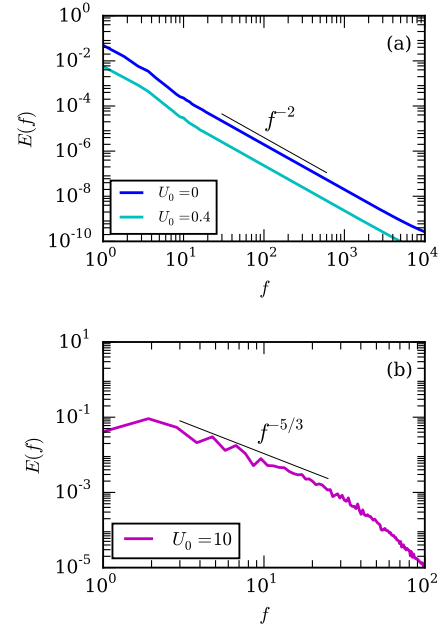


FIG. 9. For hydrodynamic turbulence simulation with  $\text{Re} \approx 1100$ , and  $\mathbf{U}_0 = 0$  and  $\mathbf{U}_0 = 10\hat{z}$ : (a) Frequency spectra  $E(f) \sim f^{-2}$  for  $\mathbf{U}_0 = 0$  and  $0.4$ ; (b) For  $\mathbf{U}_0 = 10$ ,  $E(f) \sim f^{-5/3}$  consistent with Taylor's hypothesis.



In Fig. 10 we plot the wavenumber spectrum and scaled frequency spectrum:  $f \rightarrow \tilde{f} = f(2\pi)/U_0$  and  $E(f) \rightarrow \tilde{E}(\tilde{f}) = E(f)U_0/(2\pi)$ , where  $U_0 = 10$ . We observe that both the spectra exhibit Kolmogorov's spectrum, and  $\tilde{E}(\tilde{f}) \approx E(k)$ . Thus we demonstrate consistency with the Taylor's hypothesis for hydrodynamic turbulence.

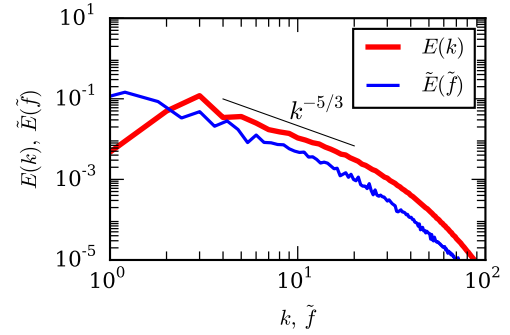


FIG. 10. For hydrodynamic turbulence simulation with  $U_0 = 10\hat{z}$ , plot of the wavenumber spectrum  $E(k)$  and scaled frequency spectrum for the real space probes:  $f \rightarrow \tilde{f} = f(2\pi)/U_0$  and  $E(f) \rightarrow \tilde{E}(\tilde{f}) = E(f)U_0/(2\pi)$ .

- 
- [1] S. Chandrasekhar, *Hydrodynamic and Hydromagnetic Stability* (Dover Publications, New York, 1961).
  - [2] J. K. Bhattacharjee, *Convection and Chaos in Fluids* (World Scientific, Singapore, 1987).
  - [3] E. Bodenschatz, W. Pesch, and G. Ahlers, *Ann. Rev. Fluid Mech.* **32**, 709 (2000).
  - [4] G. Ahlers, S. Grossmann, and D. Lohse, *Rev. Mod. Phys.* **81**, 503 (2009).
  - [5] D. Lohse and K. Q. Xia, *Ann. Rev. Fluid Mech.* **42**, 335 (2010).
  - [6] A. N. Kolmogorov, *Dokl. Akad. Nauk SSSR* **30**, 9 (1941).
  - [7] R. Bolgiano, *J. Geophys. Res.* **64**, 2226 (1959).
  - [8] A. N. Obukhov, *Dokl. Akad. Nauk SSSR* **125**, 1246 (1959).
  - [9] I. Procaccia and R. Zeitak, *Phys. Rev. Lett.* **62**, 2128 (1989).
  - [10] V. S. L'vov and G. E. Falkovich, *Physica D* **57**, 85 (1992).
  - [11] A. Kumar, A. G. Chatterjee, and M. K. Verma, *Phys. Rev. E* **90**, 023016 (2014).
  - [12] A. Kumar and M. K. Verma, *Phys. Rev. E* **91**, 043014 (2015).
  - [13] C. Sun, Q. Zhou, and K. Q. Xia, *Phys. Rev. Lett.* **97**, 144504 (2006).
  - [14] Q. Zhou, C. Sun, and K. Q. Xia, *J. Fluid Mech.* **598**, 361 (2008), ISSN 1469-7645.
  - [15] R. Kunnen, H. Clercx, B. Geurts, L. V. Bokhoven, R. Akkermans, and R. Verzicco, *Phys. Rev. E* **77**, 016302 (2008).
  - [16] Q. Zhou, C. M. Li, Z. M. Lu, and Y. L. Liu, *J. Fluid Mech.* **683**, 94 (2011), ISSN 1469-7645.
  - [17] X. Z. Wu, L. Kadanoff, A. Libchaber, and M. Sano, *Phys. Rev. Lett.* **64**, 2140 (1990).
  - [18] F. Chillà, S. Ciliberto, C. Innocenti, and E. Pampaloni, *Nuovo Cimento D* **15**, 1229 (1993).
  - [19] S. Cioni, S. Ciliberto, and J. Sommeria, *EPL* **32**, 413 (1995).
  - [20] S. Q. Zhou and K. Q. Xia, *Phys. Rev. Lett.* **87**, 064501 (2001).
  - [21] L. Skrbek, J. J. Niemela, K. R. Sreenivasan, and R. J. Donnelly, *Phys. Rev. E* **66**, 36303 (2002).
  - [22] J. J. Niemela, L. Skrbek, K. R. Sreenivasan, and R. J. Donnelly, *Nature* **404**, 837 (2000).
  - [23] X. D. Shang and K. Q. Xia, *Phys. Rev. E* **64**, 065301 (2001).
  - [24] G. I. Taylor, *Proc. R. Soc. Lond. A* **164**, 476 (1938).
  - [25] H. Tennekes and J. L. Lumley, *A First Course in Turbulence* (The MIT Press, Cambridge, Massachusetts, 1972).
  - [26] L. D. Landau and E. M. Lifshitz, *Fluid Mechanics* (Pergamon Press, Oxford, 1987).
  - [27] M. R. Cholemani and J. H. Arakeri, *J. Fluid Mech.* **551**, 19 (2006).
  - [28] X. He, G. He, and P. Tong, *Phys. Rev. E* **81**, 065303 (2010).
  - [29] G. W. He and J. B. Zhang, *Phys. Rev. E* **73**, 055303 (2006).
  - [30] B. Castaing, *Phys. Rev. Lett.* **65**, 3209 (1990).
  - [31] T. Mashiko, Y. Tsuji, T. Mizuno, and M. Sano, *Phys. Rev. E* **69**, 036306 (2004).
  - [32] S. Ashkenazi and V. Steinberg, *Phys. Rev. Lett.* **83**, 4760 (1999).
  - [33] A. Bershadskii, J. J. Niemela, A. Praskovsky, and K. R. Sreenivasan, *Phys. Rev. E* **69**, 56314 (2004).
  - [34] J. H. Arakeri, F. E. Avila, J. M. Dada, and R. O. Tovar, *Curr. Sci.* **79**, 859 (2000).
  - [35] S. S. Pawar and J. H. Arakeri, *Phys. Fluids* **28**, 065103 (2016).
  - [36] S. Grossmann and D. Lohse, *Phys. Rev. Lett.* **67**, 445 (1991).
  - [37] V. Borue and S. A. Orszag, *J. Sci. Comput.* **12**, 305 (1997).
  - [38] D. Škandera, A. Busse, and W. C. Müller, *High Performance Computing in Science and Engineering, Workshop (Springer, Berlin)* p. 387 (2008).
  - [39] F. Rincon, *J. Fluid Mech.* **563**, 43 (2006).
  - [40] P. K. Mishra and M. K. Verma, *Phys. Rev. E* **81**, 056316 (2010).
  - [41] R. Verzicco and R. Camussi, *J. Fluid Mech.* **477**, 19 (2003).

- [42] R. Camussi and R. Verzicco, Eur. J. of Mech. /B Fluids **23**, 427 (2004).
- [43] E. Calzavarini, F. Toschi, and R. Tripiccone, Phys. Rev. E **66**, 016304 (2002).
- [44] M. Kaczorowski and K. Q. Xia, J. Fluid Mech. **722**, 596 (2013).
- [45] R. M. Kerr, J. Fluid Mech. **310**, 139 (1996).
- [46] D. Nath, A. Pandey, A. Kumar, and M. K. Verma, Accepted in Phys. Rev. Fluids (2016).
- [47] J. J. Niemela, L. Skrbek, K. R. Sreenivasan, and R. J. Donnelly, J. Fluid Mech. **449**, 169 (2001).
- [48] K. R. Sreenivasan, A. Bershadskii, and J. J. Niemela, Phys. Rev. E **65**, 056306 (2002).
- [49] E. Brown, A. Nikolaenko, and G. Ahlers, Phys. Rev. Lett. **95**, 084503 (2005).
- [50] H. D. Xi and K. Q. Xia, Phys. Rev. E **75**, 066307 (2007).
- [51] P. K. Mishra, A. K. De, M. K. Verma, and V. Eswaran, J. Fluid Mech. **668**, 480 (2011).
- [52] G. Dar, M. K. Verma, and V. Eswaran, Physica D **157**, 207 (2001).
- [53] M. K. Verma, Phys. Rep. **401**, 229 (2004).
- [54] OpenFOAM, *The open source CFD toolbox*, [www.openfoam.org](http://www.openfoam.org) (2015), URL <http://www.openfoam.org>.
- [55] G. Grötzbach, J. Comp. Phys. **49**, 241 (1983).
- [56] G. Amati, K. Koal, F. Massaioli, K. R. Sreenivasan, and R. Verzicco, Phys. Fluids **17**, 1701 (2005).
- [57] R. Stevens, R. Verzicco, and D. Lohse, J. Fluid Mech. **643**, 495 (2010).
- [58] O. Shishkina, R. Stevens, S. Grossmann, and D. Lohse, New J. Phys. **12**, 075022 (2010).
- [59] See Supplementary Material at [URL will be inserted by publisher] for a movie of the convective flow at a vertical section.
- [60] A. Tilgner, A. Belmonte, and A. Libchaber, Phys. Rev. E **47**, R2253 (1993).
- [61] A. Belmonte, A. Tilgner, and A. Libchaber, Phys. Rev. Lett. **70**, 4067 (1993).
- [62] A. Maystrenko, C. Resagk, and A. Thess, Phys. Rev. E **75**, 066303 (2007).
- [63] J. Wang and K. Q. Xia, Eur. Phys. J. B **32**, 127 (2003).
- [64] C. Sun, Y. H. Cheung, and K. Q. Xia, J. Fluid Mech. **605**, 1 (2008).
- [65] G. Zocchi, E. Moses, and A. Libchaber, Physica A **166**, 387 (1990).
- [66] J. Herault, F. Pétrélis, and S. Fauve, EPL **111**, 44002 (2015).
- [67] M. K. Verma, A. G. Chatterjee, K. S. Reddy, R. K. Yadav, S. Paul, M. Chandra, and R. Samtaney, Pramana **81**, 617 (2013).
- [68] K. S. Reddy and M. K. Verma, Phys. Fluids **26**, 025109 (2014).